ChemComm

FEATURE ARTICLE

View Article Online
View Journal | View Issue



Cite this: *Chem. Commun.*, 2025, **61**, 14073

# PbS colloidal quantum dot photovoltaics: progress towards infrared and flexible applications

Sreyas M. Chintapalli,†[a] Lulin Li†[a] and Susanna M. Thon *[ab]

PbS colloidal quantum dots (CQDs) are a promising material class for near-infrared optoelectronics. The colloidal synthesis and fabrication pathways are readily scalable and compatible with a range of other materials and processes, and by controlling the size of the CQDs, the optical properties can be tuned over a wide spectral range in the visible and near-infrared (IR). This review article summarizes recent trends and advances in using PbS CQD devices for energy and photovoltaic applications. This article also provides discussion on trends in CQD research, synthesis methods, device architectures, and recent and future applications of these materials. Additionally, it describes challenges in commercialization and adoption of CQD based photovoltaics, strategies to overcome them, and perspective of the role that PbS CQDs will play in the future energy landscape.

Received 6th June 2025,
Accepted 12th August 2025

DOI: 10.1039/d5cc03198b

rsc.li/chemcomm



## 1 Introduction

Over the past century, the vast majority of society's energy needs have been met primarily through the combustion of fossil fuels and other non-renewable sources of energy.[1–3] To meet the increasing energy demands in a sustainable manner, the development of renewable sources with the capacity to produce vast amounts of energy is essential to the longevity of humanity. Of these potential sources, solar energy stands out for its abundance and ubiquity across the earth's surface.

The total solar insolation on Earth's surface eclipses any other source of energy, with recent 'reasonably assured recovery reserve' (RAR) estimates at 8300 TWYr[4] over a 30 year period, more than 12 times the expected global energy usage over this time period.[5] The standard solar spectrum on the Earth's surface, the AM1.5G spectrum, contains approximately 4.5%

[a] *Department of Electrical and Computer Engineering, Johns Hopkins University, Baltimore, MD 21218, USA. E-mail: susanna.thon@jhu.edu*
[b] *Department of Materials Science and Engineering, Johns Hopkins University, Baltimore, MD 21218, USA*
† These authors contributed equally to this work.

**Sreyas M. Chintapalli**

*Sreyas M. Chintapalli received his Bachelor's degree in Chemical Engineering from Washington University in Saint Louis in 2016. He worked as an epitaxy process engineer and photolithography engineer for finFET and silicon pressure transducer devices, respectively, until 2018. He then returned to school and received his Master's and PhD degrees in Electrical and Computer Engineering from Johns Hopkins University in 2021 and 2025, respectively. His research focuses on the intersection of machine learning, nanoparticle synthesis, device design, and fabrication, with an emphasis on using earth abundant materials and scalable fabrication methods for sustainable development of nanophotonics.*

**Lulin Li**

*Lulin Li received his Bachelor's degree in Physics in 2016 from Zhejiang University, China, and his Master's degree in Electrical and Computer Engineering in 2018 from Johns Hopkins University, where he joined the NanoEnergy Laboratory under Dr Susanna M. Thon. He received his PhD degree in 2024 also from Johns Hopkins University. His research interests include semiconductor physics, photovoltaics and renewable energy devices. Past work includes synthesis of lead sulfide (PbS) CQDs, fabrication of PbS CQD solar cells via various solution-based manufacturing methods and characterization of their optoelectronic performance.*

of incident power in the ultraviolet range (UV: 280–400 nm), 43% in the visible (VIS: 400–700 nm), and 51.7% in the near infrared range (NIR: 700–2500 nm), with a total irradiance of 1000 W $m^{-2}$.[6,7] For silicon, the most common photovoltaic absorbing material, detailed balance analysis leads to a Shockley–Queisser limiting efficiency of approximately 30%.[8–11] Approximately 19% of the incident solar power cannot be absorbed in silicon, due to the presence of photons with energies smaller than its bandgap energy in the solar spectrum, termed spectral loss.[12–15] Simply substituting silicon with a narrow bandgap material, however, leads to thermalization loss, in which electrons excited by a photon with energy higher than the bandgap quickly relax to the conduction band edge.[16–18] This means the choice of semiconductor bandgap in a photovoltaic material fundamentally limits the efficiency.

Many strategies have been proposed to overcome the Shockley–Queisser limit, including multijunction solar cells,[19–21] intermediate band cells,[22,23] up and down conversion,[24,25] hot-carrier cells,[26–28] and multiple exciton generation.[29,30] No matter the strategy, these architectures are all contingent on the development of NIR photovoltaic technologies, of which colloidal quantum dots (CQDs) emerge as a prime candidate, specifically, lead chalcogenide quantum dots.

Quantum dots are nanometer-sized semiconductor materials that are strongly quantum confined.[31–33] As the size of a nanoparticle shrinks and approaches the size of the exciton Bohr radius, the charge carriers are confined to a finite potential well in all three spatial dimensions, and the continuous energy bands in the bulk begin to discretize and increase in energetic spacing. The first exciton peak, equivalent to the bandgap in the bulk crystal, becomes size-dependent, and the bandgap widens as the particle shrinks in diameter.[34,35] Lead chalcogenide quantum dots such as PbS and PbSe have emerged as popular materials for NIR applications[36–39] due to their earth abundance and small bulk bandgaps. The desirable optical properties of quantum dots have led to their commercialization in display technologies, light emitting diodes (LEDs), and other light-emitting devices. These materials also show promise for use in light-absorbing devices such as photodetectors, phototransistors, and photovoltaics.

Colloidal quantum dots (CQDs) are synthesized in the solution phase, as opposed to vapor deposition methods[40,41] or plasma syntheses.[42,43] Colloidal synthesis allows for scalability of synthesizing quantum dots,[44,45] and large-area manufacturing processes such as roll-to-roll printing,[46,47] blade-coating,[48–50] and spray casting,[51–53] which are compatible with a variety of other materials. These liquid-based fabrication processes are not restricted to wafers or other flat surfaces and can be performed directly on flexible substrates.[54–57]

The first demonstration of a quantum dot solar cell with certified performance used a PbS CQD absorber and a ZnO electron transport layer (ETL), and was performed by Luther *et al.* in 2010, with a power conversion efficiency of 2.94%.[58] Early developments in the field centered around tuning the band alignment of the carrier transport layers and introduction of a PbS–EDT (ethanedithiol) hole transport layer (HTL).[59] Early work also focused on engineering ligand exchanges to improve charge transport in the PbS CQD layer, including the introduction of tetrabutylamonnium iodide (TBAI) and methylammonium iodide (MAI) ligands[60] leading to efficiencies of above 10% in 2015. Since then, there have been continued developments focusing around mixed halide passivation strategies for the absorbing layer, resulting in PbS–$PbX_2$ (X = I, Br, Cl) surface functionalization and PbS-perovskite structures in which the PbS quantum dots are encased with a dense perovskite matrix instead of an organic or hybrid ligand or capping agent.[61,62] Using these mixed halides increases the mobility of carriers within the absorbing layer film as well as increasing the stability of devices over time by passivating surface states on the as-synthesized quantum dots.[63] In addition to mixed-halide surface passivation, different approaches to bridging the buried interface between the quantum dot films and the transport layers to suppress non-radiative recombination in the films have been employed. Examples of this include using perovskite bridges between the quantum dots,[64] polymer layers and perovskite quantum dot interlayers,[65] and self-assembled monolayer (SAM) HTLs.[66] More recent advances include direct synthesis of PbS-mixed halide capped quantum dots and large area printing of devices.[67] In addition to this development, there has been astounding growth in the field of perovskite core quantum dots, with solar cells made from films of those materials reaching a record certified efficiency of 18.1% in a study by Aqoma *et al.*,[68] using $FAPbI_3$-MAI quantum dots. However, perovskite core quantum dots are optimized for ultraviolet and visible absorption, whereas PbS CQD solar cell efficiency gains are seen in the infrared, the spectral region we focus on for the rest of the article. A summary of the history of PbS CQD solar cell architectures and recent developments in performances are shown in Table 1.

In this feature article, we first outline the fundamentals of single junction PbS CQD solar cells, including common

**Susanna M. Thon**

*Susanna M. Thon is an associate professor of electrical and computer engineering and materials science and engineering, and the Marshal Salant Faculty Scholar at Johns Hopkins University where she also serves as the associate director of the Ralph O'Connor Sustainable Energy Institute. She received her bachelor's degree from MIT in 2005 and her Master's and PhD from the University of California Santa Barbara in 2008 and 2010, respectively, all in physics. Prior to joining Johns Hopkins in 2013, she worked as a postdoctoral fellow at the University of Toronto. Her research interests include nanomaterials engineering for optoelectronic devices, with a focus on solar energy conversion and sensing.*

 

Table 1 Major developments in single junction PbS CQD solar cells

| Architecture | $V_{oc}$ (V) | $J_{sc}$ (mA cm$^{-2}$) | FF (%) | PCE (%) | Notes | Year | Citation |
|---|---|---|---|---|---|---|---|
| ITO/ZnO/PbS–OA/Au | 0.59 | 8.93 | 55.97 | 2.94 | First certified experimental demonstration | 2010 | Ref. 58 |
| FTO/$TiO_2$ & ZnO/PbS–MPA/$MoO_x$/Au/Ag | 0.59 | 21.80 | 58.00 | 7.40 | Hybrid passivation and contact band alignment | 2012 | Ref. 69 |
| ITO/ZnO/PbS–TBAI/PbS–EDT/Au | 0.55 | 24.20 | 63.80 | 8.55 | Hole-transport layer added | 2014 | Ref. 59 |
| ITO/ZnO/PbS–TBAI/PbS–EDT/Au | 0.61 | 24.30 | 71.00 | 10.60 | MAI pretreatment of PbS–TBAI | 2016 | Ref. 70 |
| ITO/ZnO NCs/PbS–$PbI_2$/PbS–EDT/Au | 0.65 | 29.04 | 63.80 | 12.01 | PbS–$PbI_2$ halide-passivated CQDs | 2018 | Ref. 71 |
| ITO/ZnO/PbS–$PbX_2$/PbS–EDT/Au | 0.46 | 4.40 | 58.10 | 6.00 | Measurements in IR only | 2019 | Ref. 61 |
| FTO/ZnO/PbS-FAPb$Br_{3-x}I_x$/PbS–EDT/Au | 0.66 | 31.50 | 74.60 | 15.45 | Perovskite monolayer-passivated PbS CQDs | 2022 | Ref. 62 |
| ITO/ZnO/PbS–$PbX_2$/PbS–MPA/Au | 0.70 | 28.22 | 67.35 | 13.30 | Direct synthesis of PbS–$PbX_2$ inks | 2023 | Ref. 72 |
| PET/ITO/ZnO/PbS–I/PBDTTT-E-T/Ag | 0.64 | 28.27 | 61.50 | 11.04 | Flexible substrate | 2023 | Ref. 73 |
| ITO/Al:ZnO/Ag:PbS–$PbX_2$/Ag:PbS–EDT/Au | 0.63 | 29.61 | 66.70 | 12.42 | Silver-doped PbS CQDs | 2024 | Ref. 74 |
| ITO/ZnO/PbS–$PbX_2$/PbS–MPA–EDT/Au | 0.67 | 29.84 | 66.36 | 13.24 | Hybrid hole-transport-layer treatment | 2024 | Ref. 63 |
| ITO/ZnO/PbS–PEIE/PbS–EDT/Au | 0.65 | 29.60 | 69.70 | 13.40 | Polymer layer modulates trap-state loss | 2024 | Ref. 75 |
| ITO/ZnO/PbS–I/PbS–MPA/P5TCN-F25/PTAA-LAD/Au | 0.67 | 27.10 | 69.24 | 12.57 | Double-interfacial organic graded HTL | 2025 | Ref. 76 |
| ITO/ZnO/PbS–I/PbS–EDT/PBDB-T/$MoO_x$/Ag | 0.68 | 27.64 | 70.89 | 13.40 | Direct synthesis; scaled to 12.6 cm$^2$ module | 2025 | Ref. 67 |

synthesis and fabrication methods. We then summarize our recent work on spectral optimization of PbS CQD photovoltaic devices, using several techniques. Finally, we summarize recent work on PbS CQDs with the goal of using these materials to overcome the single-junction Shockley–Queisser limit, and offer a perspective on the outlook of the commercialization prospects of these materials and devices for specific applications, including challenges to be overcome and future research directions.

## 2 Size dependent properties of PbS CQDs

Lead chalcogenide (PbS, PbSe, PbTe) CQDs are the dominant CQDs in NIR applications due to their optimal tuning ranges and ease of synthesis. Particular attention has been given to PbS quantum dots, as both lead and sulfur are highly abundant elements on the Earth's surface,[77] and PbS CQDs can be synthesized with bandgaps ranging from 0.6 to 1.7 eV,[78] covering the entire range of NIR wavelengths as indicated in Fig. 1a. Several different sized PbS quantum dots' absorption spectra are shown in Fig. 1b, showing the tuning range of the first exciton peak.

The Brus equation[81] describes the theoretical modulation of the effective bandgap compared to the bulk bandgap for a quantum dot:

$$E^* = E_g + \frac{2h^2\pi^2}{D^2}\left(\frac{1}{m_e} + \frac{1}{m_h}\right) - \frac{3.6e^2}{\varepsilon_0\varepsilon_p D} \quad (1)$$

where $E^*$ is the effective bandgap, $E_g$ is the bulk crystal bandgap, $D$ is the particle diameter, $m_e$ and $m_h$ are the carrier effective masses, and $\varepsilon_p$ is the particle's relative dielectric constant. Fig. 1c gives an illustration of the quantum confinement effect as the particle diameter shrinks.[79]

Moreels *et al.*[80] showed empirically that the relationship between the effective bandgap (in eV) of a PbS CQD and its diameter, $D$ (in nm) is given by:

$$E^* = 0.41 + \frac{1}{0.283D + 0.0252D^2} \quad (2)$$

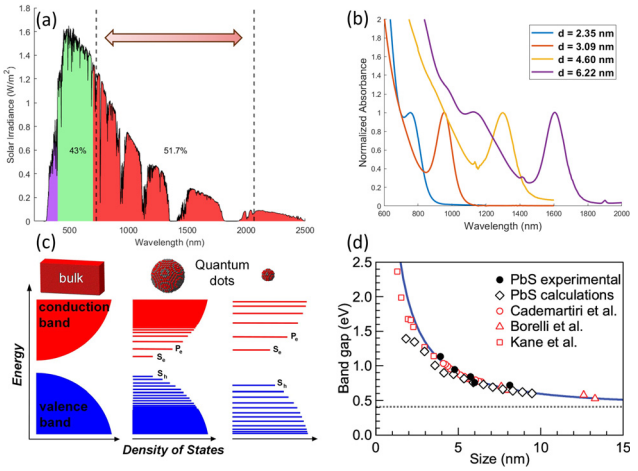


Fig. 1 Optical properties of PbS colloidal quantum dots. (a) The AM1.5G spectrum with spectral power percentages and the first exciton tuning range of PbS CQDs indicated. (b) UV-Vis-NIR absorption spectra for various sizes of PbS QDs. (c) The evolution of the band structure from the bulk to the strongly confined regime. Panel adapted from ref. 79 with permission from the American Association for the Advancement of Science, copyright 2016. (d) An empirical model for determining the bandgap of a PbS CQD from its diameter. Panel adapted from ref. 80 with permission from the American Chemical Society, copyright 2009.

This relationship was used to calculate the diameters of various synthesized dots by our group in Fig. 1b, and is plotted in Fig. 1d, along with experimental and calculated PbS CQD sizes and their respective bandgap energies reported in the literature.[82–84]

## 3 Synthesis methods

### 3.1 Hot injection

CQDs used in optoelectronics should consist of highly monodisperse nanoparticles which require the precise control of reaction conditions. The most popular CQD synthesis method is the "hot-injection method". In the case of PbS CQDs, lead oxide (PbO) and oleic acid (OA) are often selected as the lead

source and coordinating ligands, respectively. The mixture is heated under vacuum to form lead oleate. Next, the bis(trimethylsilyl) sulphide [$(TMS)_2S$], the sulfur source, is quickly injected into the solution, leading to a rapid nucleation process forming monodisperse nanoparticles. Nucleation is indicated by a color transition in the solution from colorless to dark during the injection process.[85] By varying the reaction factors such as precursor concentration, injection temperature and post-treatment methods, the size of CQDs, which directly corresponds with the bandgap value, can be tuned.[86]

Another simple synthesis method is called the ''heating-up method'', indicating that all precursors are mixed at a low temperature and heated together to a specific target temperature. This method is easier to control compared with the delicate injection required of the previous method. The heating-up method is also a one-pot synthesis with high yield. However, the size distribution of the CQDs produced through this method may not be as monodisperse as desired.[87,88]

### 3.2 Direct synthesis

While the hot injection method provides quantum dots with long-term shelf stability and excellent size control,[89] the stabilizing oleic acid ligands need to be replaced with different capping agents to produce efficient optoelectronic devices, as further discussed in Section 4. More recently, there have been a variety of direct synthesis methods in which these surface-functionalized quantum dots are synthesized and then immediately made into the absorbing layer, bypassing a ligand-exchange step.[90] In this method, $PbI_2$ and diphenyl thiourea (DPhTA) are dissolved in dimethyl formamide (DMF), without the need for degassing. Next, butylamine (BA) is quickly injected at room temperature, and the PbS CQDs nucleate. Butylamine is suspected to be a temporary ligand that facilitates the growth of PbS–PbI nanoparticles, which are one of several common surface-functionalized PbS quantum dot variants used in photovoltaic devices. Even more recently, Ding *et al.* have shown that beginning with mixtures of $PbI_2$ and other halogenated lead salts such as $PbBr_2$ and $PbCl_2$ can further improve device performance, likely due to increased charge transport in the film phase after direct synthesis of the mixed lead halide PbS–$PbX_2$ (X = Cl, Br, I) quantum dots.[91]

### 3.3 Microwave assisted synthesis

Microwave assisted synthesis has also been used for NIR quantum dots.[92,93] Here, lead and sulfur precursors are stirred vigorously in ambient conditions under high power microwave radiation (400 W) for 2 minutes, causing a rapid change in temperature. During this step, PbS CQDs form and begin to aggregate into microstructures. After this, the reaction vessel is allowed to cool to room temperature and more solvent is added, diluting the remaining precursors. Next, another low power (40 W) microwave step is used to irradiate the vessel for 1 minute. Finally, an ultrasonication step breaks the weakly bound microstructures into PbS CQDs. This method produces slightly wider size distributions than the hot-injection method, but has appeal in scaling CQD fabrication, since the entire processes happens on the order of minutes as opposed to hours.[92]

## 4 Surface functionalization

Surface ligands are crucial in CQD synthesis processes and post treatments. For the purposes of liquid-phase synthesis and long-term storage, long chain organic ligands are chosen to keep the colloidal system stable and avoid aggregation. Critically, the long chain organic ligands also play the role of passivating electronic trap states.[94,95] However, in the processes of thin film formation and device fabrication, these long-chain and insulating organic ligands act as electronic tunneling barriers, resulting in decreased charge transport rates. Therefore, ligand exchange strategies to shorter and conducting molecules are important for CQD optoelectronic device fabrication.

Conventional layer-by-layer solid-state ligand exchange strategies, in which solutions of shorter ligands are introduced onto preformed solid state films, have largely been replaced by solution-phase ligand exchange strategies. These strategies have advantages including more complete removal of the long-chain synthesis ligands and more thorough trap state passivation.[96] Moreover, solution-phase ligand exchange strategies enable single-step deposition methods which reduce or eliminate the large material waste associated with layer-by-layer multi-step film formation strategies that utilize solid-state ligand exchange methods.

In the solution-phase ligand exchange strategy, the exchange process is carried out in the liquid state *via* a phase transfer process, directly replacing the long insulating organic ligands with short conducting ones, forming a ready-to-use CQD ink.[97] During the preparation of the CQD ink, metal halides such as lead iodide ($PbI_2$) or lead bromide ($PbBr_2$) are used to replace the long oleic acid (OA) ligands. The metal halide is dissolved in dimethylformamide (DMF) and added into the OA-capped CQD octane solution. After mixing and centrifuging, the CQDs transfer from the non-polar solvent (octane) into the polar solvent (DMF), producing halide-capped CQDs. These shorter ligands ultimately lead to enhanced electronic coupling between neighboring CQDs in the film phase.

The single-step deposition process used for the solution-phase ligand-exchanged CQDs typically requires a compatible fast-drying solvent. Initially, butylamine (BTA) was used; however, BTA is highly polar, leading to unstable PbS CQD solutions and limiting the scale-up of CQD film deposition.[98] The hybrid amine strategy, consisting of a mixture of BTA, amylamine and hexylamine, was therefore studied to improve the stability of the CQD ink, potentially increasing the photovoltaic device efficiency.[71,96] In general, the solution-phase ligand exchange strategy has proven to be a crucial development in advancing PbS CQD film quality and optoelectronic device performance.

## 5 Single junction PbS CQD solar cells

### 5.1 Charge transport layer engineering

CQD solar cells have experienced rapid performance increases, from their first certified power conversion efficiencies (PCEs) of 2.9% in 2010 to over 18% today.[99,100] The most widely-used photovoltaic device architecture is based on a heterojunction solar cell with an p–i–n device structure. In this architecture,

 

ZnO is used as the electron transport layer (ETL), the photoactive (absorbing) layer consists of a thin film of PbS CQDs with $PbX_2$ (X = I, Br) ligands prepared from a CQD ink, and a PbS CQD film with ethanedithiol (EDT) ligands deposited *via* a solid-state exchange process acts as the hole transport layer (HTL).

The basic structure of a single junction PbS CQD solar cell device is shown in Fig. 2a.[101] The bottom-illuminated solar cell structure includes a transparent conductive electrode, an n-type electron transport layer, an absorbing layer in which incident photons excite charge carriers, a p-type hole transport layer, and a top metal electrode. In practice, positive and negative charge carriers are generated in the absorbing layer, and separately transported into the top and bottom electrodes *via* the hole transport layer and the electron transport layer, respectively.

ZnO is a popular electron transport layer material due to its optical transparency and electron affinity alignment with 1.3 eV bandgap PbS CQD thin films. However, the ZnO layer plays a crucial role in determining experimental yields and repeatability. Chiu *et al.* presented a comprehensive study of ZnO recipes used for the electron transport layers in PbS CQD solar cells to discover their effects on the yield of working devices.[102] Generally, the mixture of zinc acetate and potassium hydroxide was heated for a desired heating time to form the ZnO nanoparticles. The study found that the optimal heating time of the ZnO synthesis process should be 2 hours and 40 minutes to achieve high performance and high device yield at the same time. The study also determined that the dispersion solvent was a crucial factor for high yields and high performance CQD solar cells. Among the final solvent choices for the ZnO nanoparticle electron transport layer, a chloroform : methanol ratio of 1 : 1 led to high performance and achieved the highest device yield. Simultaneously achieving high performance and high device yields should be a critical factor in the industrialization and commercialization process of PbS CQD solar cells for potential applications in multi-junction solar cells, color-tuned solar cells, and flexible and wearable devices.

The ethanedithiol (EDT) solid-state ligand-exchanged PbS CQD hole transport layer exhibits relatively low carrier mobility and doping density. Therefore, it is considered a limiting factor in achieving high device performance. Chiu *et al.* developed an optimized hole transport layer composition, which showed improved p-type characteristics *via* sulfur surface passivation and, therefore, improved photovoltaic performance.[101] In this work, elemental sulfur was infused into the conventional PbS–EDT hole transport layer *via* electron beam evaporation, as shown in Fig. 2b. This study found that the improved electron mobility that resulted was the key factor in the improved PCE. Although electron mobility in a hole transport layer is not typically considered important, this result led to the discovery that a nontrivial amount of photogeneration was occurring in the hole transport layer, and the improved ability to extract electrons from this layer therefore played a role in improved device performance, as shown in Fig. 3. Mobility measurements were carried out using the space-charge limited current (SCLC) method.[103] The average PCE (taken over 50 devices) increased from 9.3% to 10.4%, a considerable improvement in performance. The sulfur surface passivation strategy demonstrated the importance of engineering the CQD absorbing layer composition, to further rectify surface trap states and sulfur vacancies.[104]

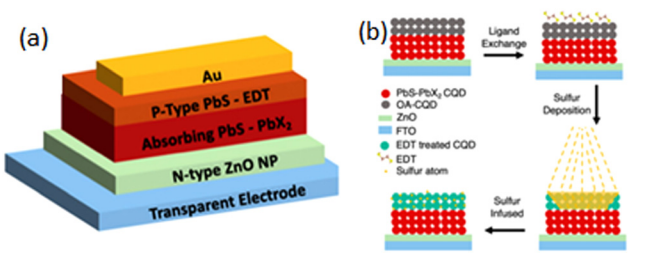


Fig. 2 A PbS CQD solar cell. (a) Schematic of a conventional PbS CQD solar cell. (b) Diagram of a sulfur-doped hole transport layer fabrication process used to improve charge carrier mobilities. Reproduced with permission from ref. 101 from American Chemical Society, copyright 2020.

### 5.2 Next-generation characterization methods

As device performance in CQD solar cells improves, there is a need for new advanced characterization methods to understand the local properties of PbS CQD films, particularly with an eye towards commercialization and scale-up. Recently, Lin *et al.* demonstrated a micrometer-resolution 2D characterization method with a millimeter-scale field of view.[105]

The system, which consists almost entirely of off-the-shelf instrumentation, can generate high-resolution mappings over large areas by scanning the excitation over the active area and simultaneously measuring multiple optoelectronic properties of interest. The system design is shown in Fig. 4a, with an atomic force microscopy (AFM) map and photograph of a CQD solar cell shown in Fig. 4b and c, respectively. The excitation source is a pulsed laser, and the device is mounted on an $x$–$y$–$z$ translation stage with sub-micron resolution. It is capable of synchronous and aligned measurement of photoluminescence spectra, transient photocurrent and photovoltage responses, full current–voltage curves, and other optical and electronic characteristics. The system provides spatially correlated maps of these parameters, allowing for deep insight into how defects and inhomogeneity impact device performance. This system works not only for sub-micron-scale defects, but also for macroscale inhomogeneities that are often visible to the eye. These are typically accidentally introduced during the fabrication process, and can be attributed to dust particles, agglomerates precipitated during solution-processing, and random scratches incurred during testing.

Fig. 5 shows several spatially-resolved maps of solar cell properties that were acquired simultaneously for two different CQD devices. Fig. 5a–c contain photoluminescence, transient photocurrent, and transient photovoltage measurements which can be used to calculate limiting carrier mobilities[106] and mid-gap trap state densities[107] through the following procedure, starting with calculating the change in charge from a pulsed

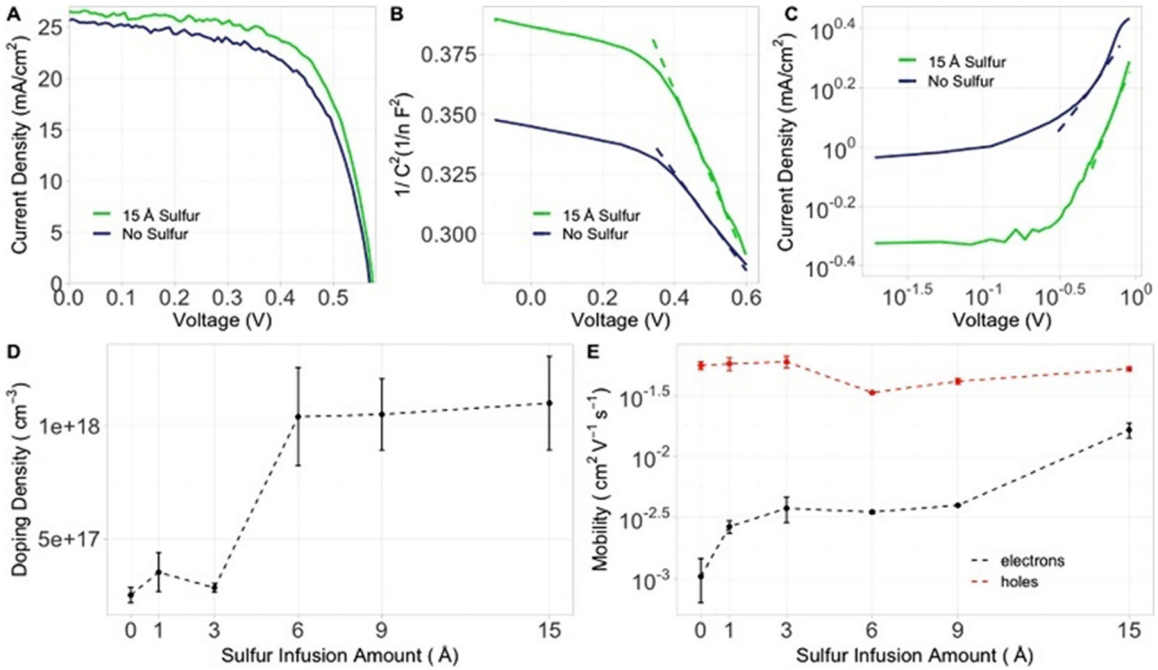


Fig. 3 Improvements in device performance from sulfur treatment of the HTL. (a) Current density–voltage plots of the best performing control HTL device (purple) and a 15 Å sulfur HTL device (green). (b) Capacitance–voltage (Cap–*V*) measurements of a control HTL device (purple) and a 15 Å sulfur HTL device (green), and the linear fits used to extract the doping densities (dashed). (c) Current density–voltage log plot of an electron-transport SCLC structure control HTL device (purple) and a 15 Å sulfur HTL device (green), with the SCLC region, used to calculate the electron mobility, indicated by dashed lines. (d) Average doping density in the HTL extracted from Cap–*V* measurements as a function of sulfur infusion amount. (e) Hole mobility (red) and electron mobility (black) extracted from SCLC measurements as a function of sulfur infusion amount. Reproduced with permission from ref. 101 from American Chemical Society, copyright 2020.

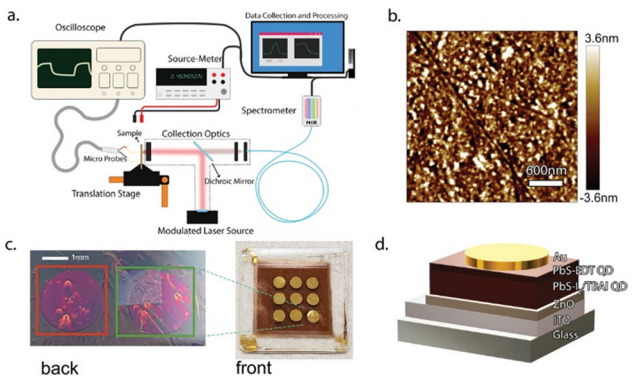


Fig. 4 Multimodal scanning system for local defect characterization. (a) Diagram of the multi-modal measurement and data collection system. (b) AFM image of a 3 × 3 μm² area of the surface of a CQD photovoltaic device, showing a root-mean-square average local roughness of 2.6 nm. (c) Left: Photograph of two of the PbS CQD solar cell devices, defined by circular top contacts of 2.4 mm in diameter, taken through the glass substrate (''back''). Right: Photograph of the entire PbS CQD solar cell substrate with 9 devices (''front''). (d) Diagram of the full device architecture. Reproduced with permission from ref. 105, 2020 WILEY-VCH Verlag GmbH & Co. KGaA, copyright 2020.

photocurrent measurement:

$$\Delta Q = \int I(t)\mathrm{d}t \tag{3}$$

where $I(t)$ is the photocurrent measured across a 50 Ω shunt resistor. Next, the transient photovoltage signal can be fit to the following equation:

$$\Delta V_{\mathrm{oc}}(t) = \Delta V_{\mathrm{oc}}(0)\exp\left(-\frac{t}{\tau_{\mathrm{s}}}\right) \tag{4}$$

where $\Delta V_{\mathrm{oc}}(0)$ is the change in the initial transient photovoltage amplitude and $\tau_{\mathrm{s}}$ is the time constant, a fit parameter. Using these equations together, the differential capacitance, $C$, can be calculated from:

$$C = \frac{\Delta Q}{\Delta V_{\mathrm{oc}}(0)} \tag{5}$$

Integrating this up to a particular open-circuit voltage gives an estimate of the mid-gap trap state density, $n$:

$$n = \frac{1}{Aed}\int_0^{V_{\mathrm{oc}}} C\mathrm{d}V \tag{6}$$

where $A$ is the device area, $e$ is the fundamental electron charge, and $d$ is the device thickness. The system also exhibits the capability of producing the large datasets required to build a training library for input into machine learning algorithms, with the goal of locally predicting how defects will affect optoelectronic performance from simple imaging. Once a sufficiently sized dataset of ~7000 samples is collected, as opposed to 10 000 s in other supervised machine learning-based models,

 

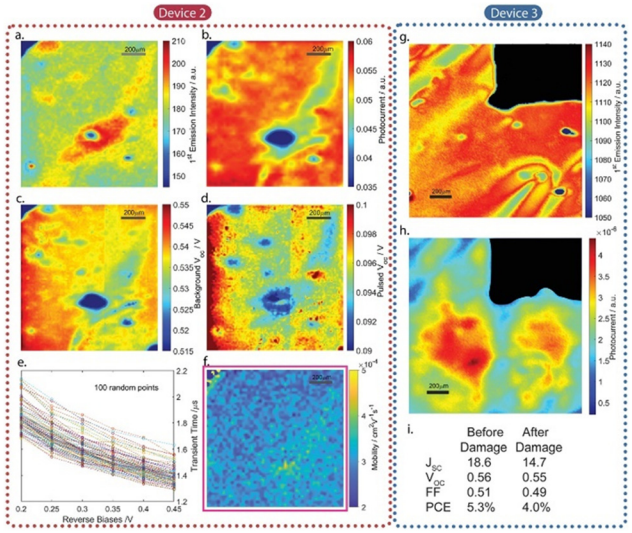


Fig. 5 (a) Core state photoluminescence intensity map for a CQD solar cell taken using the multimodal scanning instrument. (b) Transient photocurrent amplitude map. (c) Background transient photovoltage amplitude map. (d) Pulsed transient photovoltage amplitude map. (e) Charge carrier transit time extracted from transient photocurrent measurements as a function of reverse bias, from 100 random points within the same area. (f) Carrier mobility map obtained from the transient photocurrent measurements. (g) Core state photoluminescence intensity map for a device (device 3) that was intentionally damaged *via* high intensity laser irradiation in the upper right corner. (h) Photocurrent amplitude map for device 3. (i) Solar cell figures of merit for the entirety of device 3 before and after the intentional laser irradiation-induced damage. Reproduced with permission from ref. 105, 2020 WILEY-VCH Verlag GmbH & Co. KGaA copyright 2020.

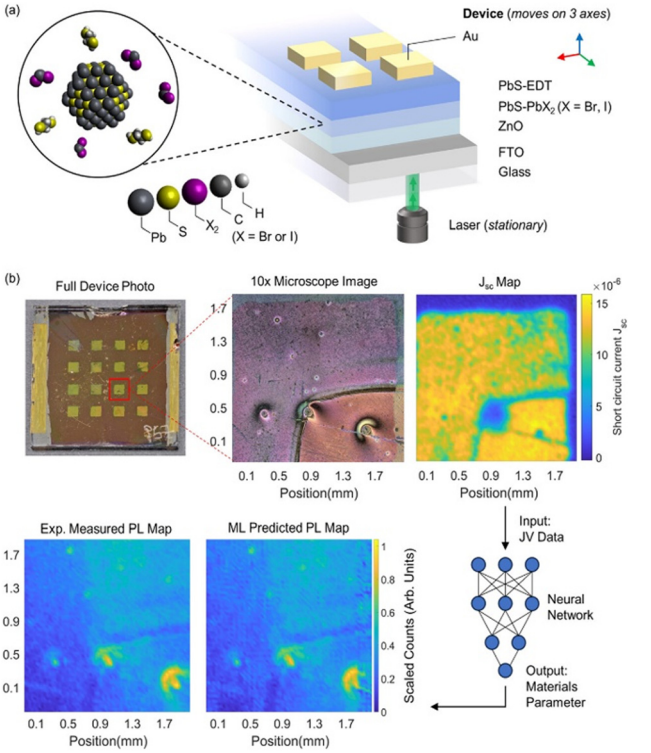


Fig. 6 (a) Layer composition of the PbS CQD photovoltaic devices used in this study, including a schematic of the atomic structure of a PbS CQD and associated surface ligands. The device structure consists of a glass substrate, a fluorine-doped tin oxide (FTO) transparent conductive electrode, a ZnO electron-transport layer, a PbS CQD thin-film absorbing layer with PbX (X = Br, I) ligands (PbS–$PbX_2$), a PbS CQD hole-transport layer with ethanedithiol ligands (PbS–EDT), and patterned gold electrodes defining the device areas. (b) Top left: Photograph of a substrate containing 16 solar cell devices. Top middle: Microscope image (10× magnification) of the device indicated by the red box. Top right: Measured short-circuit current map of the device. The edge of the device, defined by the gold electrode, can be seen in the current map as a transition from yellow/green active area to blue inactive area. Bottom left: Experimentally measured *versus* network predicted photoluminescence map of the same device. Reproduced with permission from ref. 109, Wiley-VCH GmbH, copyright 2024.

mobilities and trap state densities can be estimated from simple JV measurements, allowing for high-throughput characterization of PbS CQD, or other 3rd generation, photovoltaic cells.[108] Lee *et al.* showed, through use of residual neural networks, that from a simple JV measurement of a PbS CQD solar cell, many of the underlying material properties can be predicted from a small library of substrates.[109] An overview of the entire system, with the machine-learning enhanced capabilities, is shown in Fig. 6.

In the future, this method could be harnessed to develop a universal predictive model that automatically extracts all essential optoelectronic parameters from simple *J–V* curve measurements, independent of the materials system or device configuration—paving the way for broader applications of intelligent systems in device development.

# 6 PbS CQD devices for novel applications

## 6.1 Color-tuned solar cells

Custom solar cells are an attractive option for building-integrated photovoltaics (BIPV), where the design of the building envelope includes solar cells, as opposed to a rooftop system installed at a later point in time.[110,111] Arinze *et al.* developed a method to customize the color of PbS CQD solar cells through optical interference effects by tuning the thicknesses of the solar cell layers.[112] In combination with advances in spray-casting colloidal solar cells,[51] this opens up many more market possibilities for CQD inks. The p–i–n structure (Fig. 7a) and SEM cross section (Fig. 7b), and a schematic of the optimization routine for color tuning is given in Fig. 7c. In this color optimization technique, an initial starting point of thicknesses for the ETL, absorbing layer, and HTL is set. Then, using the transfer matrix method (TMM), the reflection spectra of the full stack is calculated, and mapped onto the RGB color space on a chromaticity chart. The particle swarm optimization algorithm is then used to generate the next set of thicknesses, and the procedure is iterated until the thicknesses are optimized for a given color in reflection or transmission.[113]

Post optimization, the relevant optical and electronic characterization of experimental devices (Fig. 7d–f) along with several custom-colored cells (Fig. 7g) are shown. This technique achieved a full range of colors, as well as a semi-transparent

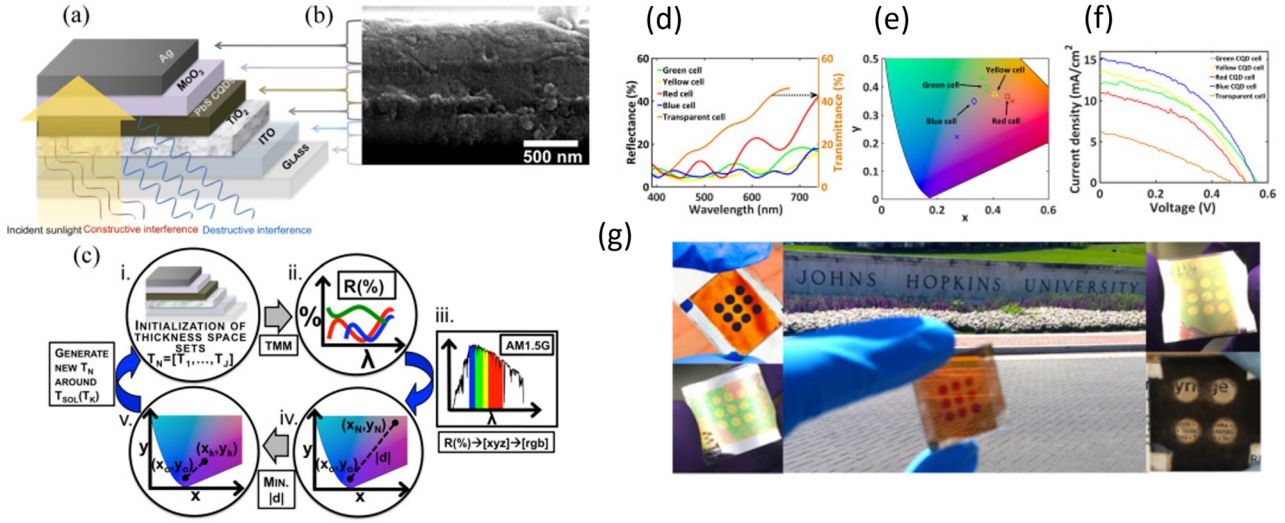


Fig. 7 Color tuned PbS CQD solar cells. (a) Schematic of a CQD solar cell illustrating the spectrally-dependent optical interference patterns that can result from tuning the thicknesses of the different cell layers. (b) Cross-sectional scanning electron microscope (SEM) image of the structure shown in (a) with the layers labelled. (c) Optimization technique: the space set of thickness combinations is (i) initialized and each combination is transformed to (ii) a reflection spectrum *via* TMM. These spectra in combination with incident (iii) AM1.5G and color matching functions are translated to RGB colors on (iv) chromaticity plots where the distance to the intended color is (v) minimized. (d) Experimental reflectance and transmittance spectra for colored and semi-transparent solar cells, respectively. (e) Chromaticity plot showing the calculated coordinates for different colored devices. Crosses indicate design points while corresponding colored shapes indicate experimental points. (f) *J*–*V* characteristics taken under simulated solar illumination for colored and semi-transparent devices. (g) Photographs of blue (upper left), green (lower left), red (center), yellow (upper right), and semi-transparent (lower right) CQD solar cells. Reproduced with permission from ref. 112, Optical Society of America, copyright 2017.

device. In addition to color-tuning, PbS CQD solar cells are well suited to a plethora of designs, including deposition on curved surfaces, unlike existing BIPV technologies.[111,114] The range of flexibility in the designs and architectures for CQD photovoltaic devices enables them to be prime candidates for a wide variety of applications in the emerging fields of indoor photovoltaics[115] and in the pursuit of net-zero buildings and homes.

### 6.2 Spectrally selective films

In addition to color-tuning, PbS CQD films can be patterned to alter their spectral properties in more complex ways. A desirable property in photovoltaic films is having a finite absorption bandwidth, for applications such as enabling current-matching in multi-junction solar cells. While typical semiconductors have an absorption onset, patterning a semiconductor-like film can prevent certain modes from propagating through the film into guided modes within the plane of the film, using concepts from the field of photonic crystals.[116]

This type of patterning can be realized with scalable fabrication techniques such as nanosphere[117] or nano-imprint lithography[118] over large areas, which is crucial for photovoltaics. Fig. 8 shows a theoretical and experimental realization of spectral modulation and selectivity in PbS CQD films. Fig. 8a illustrates the idea, where the out-of-plane incident light couples to in-plane guided modes, with the corresponding band diagram and out-of-plane absorption and transmission spectra. Fig. 8c and d show a simulated and experimental realization of a PbS CQD film with a modified photonic band structure. Fig. 8e and f show two in-plane electric field profiles at two different wavelengths within the slab, showing constructive and destructive interference effects due to the patterning (Fig. 8g). Fig. 8h shows simulation results for a model system composed of a patterned semiconductor with a real constant dielectric constant of $\varepsilon = 13$ and a triangular lattice of air-holes with a normalized radius of $r = 0.24a$, and a normalized thickness of $t = 0.5a$, where $a$ is the lattice constant. The blue and yellow-dashed lines represent the transmission and reflection spectra of the structure. The red and purple-dashed lines represent the same transmission and reflection spectra, but here with the background slab material having a complex dielectric function of $\varepsilon = 13 + 0.26j$. The imaginary part of the dielectric function must be included for absorbing materials such as PbS CQD films, unlike what is assumed in typical photonic band structure calculations. Note that although the resonances and coupling between guided modes and the out-of-plane spectral features become less sharp, the spectral position of the features does not change with the presence of absorption in the medium.

In the traditional design process for structured materials such as those used to make spectrally-selective PbS CQD films, a designer draws and simulates a thin-film structure using a physics-based algorithm such as the finite-difference time-domain method (FDTD) or rigorous coupled wave analysis (RCWA). These calculations are computationally expensive, and to realize a target absorption or transmission spectrum, there needs to be an extensive iteration process between the design and calculation steps. Recently, inverse design methods[119–121] based on machine learning and neural-network models have

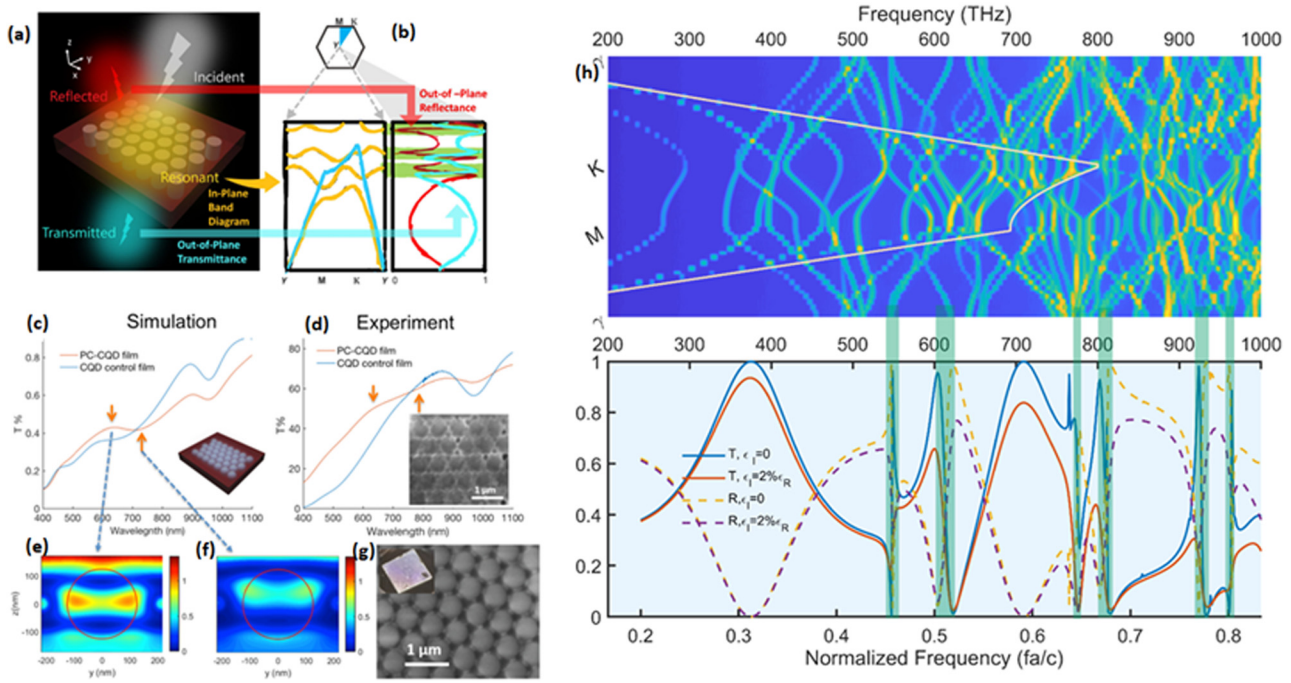


Fig. 8 (a) Illustration of a patterned semiconductor slab showing the coupling between out-of-plane spectral features with the in-plane guided modes. (b) A hexagonal unit cell with the corresponding band diagram and normal incidence reflectance, transmittance, and absorption spectra. (c) Simulated and (d) experimental spectra for un-patterned and patterned CQD films, demonstrating modulation of the transmission spectrum. The inset is an SEM image of the film (scale bar is 1 μm). (e) and (f) Two simulated electric field profiles at two different wavelengths for a patterned CQD slab. (g) SEM image of a polystyrene nanosphere array used to create the patterned structure. (h) Fourier modal method-calculated transmission (solid lines) and reflection (dashed lines) spectra (bottom) for a triangular lattice slab photonic crystal with hole radius $r = 0.24a$, thickness $t = 0.5a$, dielectric constant $\varepsilon = 13$ (blue and yellow spectra), and complex dielectric function $\varepsilon = 13 + 0.26j$ (red and purple spectra); $a$ is the period. The incident field is perpendicular to the slab structure. The corresponding finite-difference time-domain method-calculated photonic band structure for the $\varepsilon = 13$ case is shown in the top panel (light line plotted in white). The resonance regions are highlighted and associated with the modes at the $\gamma$-point in the photonic band structure. Reproduced with permission from ref. 116, Optical Society of America, copyright 2018.

been demonstrated for creating structures from desired spectra in an "inverse" process, as opposed to the forward-design method described above. These methods were initially used for photonic waveguide design and in non-absorbing media.

Chintapalli *et al.* applied inverse design methods for broadband enhancement of absorption in the NIR and enhancement of transmission in the UV-vis in PbS CQD films, which is an ideal spectral scenario for a multi-junction solar cell configuration with a PbS CQD-based top NIR cell. Fig. 9 shows an example of the mapping between randomly generated unit cells and the predicted spectra based on a supervised convolutional neural network (CNN), with ~99.9% accuracy between the CNN model and physics-based algorithms. This calculation takes less than a second, as opposed to 10 s of minutes for a traditional FDTD calculation per design. Inverse design methods are promising for making highly customizable spectral responses in PbS CQD films.

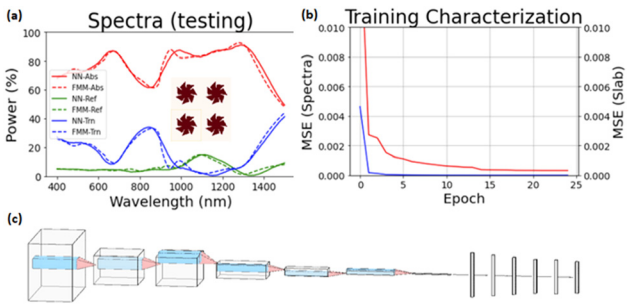


Fig. 9 (a) A comparison of CNN trained (solid) and Fourier modal method (dashed) calculated absorption (red), transmission (blue), and reflection (green) spectra, for the unit cell in the inset (dark red represents PbS CQDs, with the lighter area being air). (b) The testing characterization of the CNN for recovering the spectra (red) and slab parameters – lattice constant and slab thickness (blue). (c) An illustration of the CNN which functions as an image encoder, converting the 64 × 64 pixel image of the unit cell, and two scalar slab parameters into the three spectra (221 length vectors) and recovering the two scalar slab parameters. Adapted with permission from ref. 121, Institute of Electrical and Electronics Engineers, copyright 2023.

### 6.3 Tandem solar cells

Tandem solar cells (TSCs) are multi-junction solar cells with two p–n junctions, typically consisting of materials with two different band gaps. Employing additional junctions is a successful strategy for overcoming the single-junction Shockley–Queisser limit, and the theoretical maximum efficiency of a TSC is 42%.[122] PbS CQD films are well-suited as the narrow bandgap absorbers in tandem devices. The absorption onset of PbS CQD films can be readily tuned from 0.75–1.6 eV (775–1550 nm).[80,95] Compared to silicon ($E_g$ = 1.12 eV), which is used

Table 2 Tandem solar cell demonstrations incorporating PbS CQD films

| Front cell, recombination layer, rear cell | Front absorber, terminals, rear absorber | $V_{oc}$ (V) | $J_{sc}$ (mA cm$^{-2}$) | FF (%) | PCE (%) | Year | Ref. |
|---|---|---|---|---|---|---|---|
| ITO/PbS CQD, **Al/$WO_3$**, P3HT:$PC_{61}BM$/Al | CQD, 2T, organic | 0.89 | 3.9 | 58 | 1.02 | 2014 | Ref. 130 |
| FTO/$TiO_2$/PbS–MPA, **MoOx/ZnO**, PFN/PTB7-th:$PC_{71}BM$/$MoO_3$/Ag | CQD, 2T, organic | 1.25 | 6.12 | 69.2 | 5.33 | 2015 | Ref. 134 |
| ITO/InZnO/PbS–I/PbS–EDT/$MoO_3$, **Au**, ZnO NP/PTB7-th:$PC_{71}BM$/$MoO_3$/Ag | CQD, 2T, organic | 1.25 | 9.89 | 74.1 | 9.12 | 2017 | Ref. 96 |
| ITO/$TiO_2$/PbS/$MoO_3$, **ITO/AZO**, $TiO_2$/PbS–I/Au | CQD, 2T, CQD | 1.06 | 8.3 | 48 | 4.21 | 2011 | Ref. 19 |
| ITO/s-ZnO/PbS–TBAI/PbS–EDT, **Au-PEDOT**, ZnO NP/PbS–TBAI/PbS–EDT/Au | CQD, 2T, CQD | 1.13 | 12.26 | 64.1 | 8.9 | 2017 | Ref. 132 |
| ITO/ZnO NP/PbS–I/PbS EDT, **Au**, ZnO NP/PbS–I/PbS EDT/Au | CQD, 2T, CQD | 1.07 | 11.5 | 55 | 6.8 | 2019 | Ref. 133 |
| ITO/ZnO NP/PbS–TBAI/PbS–EDT, **n-PEDOT/$SnO_2$ NP**, $MaPbI_3$/spiro-OMeTAD/$MoO_3$/Ag | CQD, 2T, Perovskite | 1.66 | 8.91 | 74.6 | 11.03 | 2018 | Ref. 126 |
| ITO/ZnO NWs/$SnO_2$/$(FAPbI_3)_{0.92}(MAPbBr_3)_{0.08}$/CuPC, **Au/$MoO_3$/ITO**, ZnO NP/PbS QDs/Au | CQD, 2T, perovskite | 1.55 | 16.3 | 69 | 16.96 | 2021 | Ref. 127 |
| FTO/ITO/$SnO_2$ NP/Cs(MA)(FA)(PbI)Br/$MoO_3$/Ag/$MoO_3$, ITO/AZO/PbS–$X_2$/PbS–EDT/Au | CQD, 4T, perovskite | — | — | — | 20.2 | 2019 | Ref. 129 |
| FTO/c-$TiO_2$/m-$TiO_2$/$MAPbI_3$/Spiro-OMeTAD/Au, ITO/ZnO NP/PbS–$X_2$/PbS–EDT/Au | CQD, 4T, perovskite | — | — | — | 15.93 | 2021 | Ref. 128 |

as the IR absorber in popular perovskite/silicon tandem cells, PbS CQDs can access an additional 101.3 W m$^{-2}$ – over 10% – of the AM1.5G spectrum. The band gap tunability allows for these films to be compatible with a wide range of other single-junction architectures such as: amorphous silicon,[123] dye-sensitized cells,[124,125] perovskites,[126–129] organic,[96,130,131] and other size-tuned CQDs.[132,133] Table 2 lists several tandem demonstrations involving PbS CQD films and their associated performances.

A critical technology needed for a high performance TSC is the recombination layer (RL). In the typical design for 2 terminal (2T) TSCs, the bottom cell is a narrow bandgap junction meant to collect NIR light, while the top cell is a wide band gap junction used to absorb visible light and transmit the NIR light. In order to connect the two cells in series and achieve voltage addition, electrons generated from the back cell must recombine with holes generated from the front cell, requiring a recombination layer or tunnel junction.[19] A second engineering consideration for TSCs is current-matching between the bottom and top cell, as the photocurrent generated by two series-connected solar cells will be limited to the lower of the two cell's photocurrent.[12] Given these two design requirements, CQD TSCs often employ a graded recombination layer (GRL) which matches the band energies in the respective cells, allowing carriers to recombine while minimizing voltage loss. This is coupled with optimization of the other layer thicknesses in the cell to achieve current-matched conditions.[12,122,123] In Table 2, the recombination layer materials that have been used in past demonstrations of TSCs incorporating PbS CQD films are highlighted in bold in the first column. There are a myriad of choices and classes of materials that can be used, and finding the ideal RL for a given architecture remains a challenge in the field. Despite this challenge, the compatibility of PbS CQD films with many other solution-processed materials and films continues to make them a prime candidate for the IR cell in hybrid TSCs.

### 6.4 Spray cast and flexible devices

Given the solution-processed nature of CQDs, it is feasible to fabricate solar cell devices upon flexible substrates, making it possible to expand the use scenarios towards wearable devices, mobile devices or transportation tools. Li *et al.* developed a spray-cast manufacturing method to demonstrate flexible PbS CQD solar cells.[135] In this demonstration, the crystalline transparent conductive oxide bottom electrode and the evaporated gold top electrode were replaced by spray-cast silver nanowire networks initially dispersed in isopropanol.[51] Therefore, all layers of the solar cell began as liquid-phase materials, and an entire cell could potentially be spray-cast onto nearly any substrate. The film quality and thickness in the study could be tuned by adjusting spray parameters such as air pressure, spray time, and substrate temperature.

Fig. 10a shows a comparison of the modified spray-cast PbS CQD solar cell structure to the conventional structure. For a fully spray cast solar cell, silver nanowires make up both the top and bottom contact layers, which allows for tunability in the transparency of the films, as well as sufficient conductivity. The transmission curves shown in Fig. 10b illustrated that the best-performing spray-cast silver nanowire electrode provides transparency comparable to traditional transparent conductive oxide products, such as indium-doped tin oxide (ITO) and fluorine-doped tin oxide (FTO) in the visible range, while maintaining

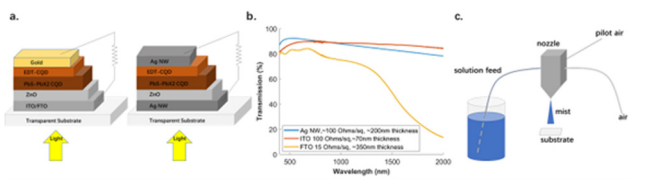


Fig. 10 (a) (left) Schematic of a conventional PbS colloidal quantum dot solar cell structure and (right) a fully spray-cast colloidal quantum dot solar cell structure. (b) Transmission curve comparisons between best-performing spray-cast silver nanowire transparent electrode and conventional transparent conductive oxide samples. (c) Schematic of the spray-casting instrument. Air is supplied to trigger the siphon effect that pushes the liquid solution into the nozzle, and the spray-casting process commences. The pilot air is controlled by pneumatic valves which are used to turn on/off the nozzle. Adapted with permission from ref. 135, Institute of Electrical and Electronics Engineers, copyright 2023.

 

an acceptable conductivity. A diagram of the spray-casting instrument is shown in Fig. 10c. This type of system could be scaled to produce commercial films, and future work will involve incorporating ultrasonic activation into the instrument, which could allow for finer control of film properties.

## Conclusions

With growing interest in new applications for solar energy harvesting, PbS CQDs remain an intriguing material for extending solar responsivity to and beyond the NIR. Here, we summarized some of the unique properties that have allowed PbS CQDs to be integrated with a wide range of other materials in tandem solar cells, deployed on curved and flexible surfaces for applications such as wearables or building-integrated photovoltaics, and used as spectrally-tuned materials through several novel design and fabrication processes. There are a few key areas that will need continued research and development along the path to commercial deployment of these devices:

(1) Charge carrier transport layer engineering. While there have been many successful strategies to improve transport and electrical performance in PbS CQD solar cells, the electron and hole transport layers still remain limiting factors in device performance, due to deficiencies such as sub-optimal energy band alignment with the PbS CQD absorbing layer and contacts, limited doping densities, and limited charge carrier mobilities. Many recent advances in these transport layers have relied on traditional semiconductor processing methods, such as chemical vapor deposition, that may be incompatible with scalable manufacturing techniques for PbS CQD solar cells, due to requiring low pressures and elevated temperatures. Measuring the valence and conduction band energies in the charge transport layers or recombination-suppressing polymer layers through techniques such as ultraviolet photoelectron spectroscopy (UPS) can help eliminate or validate various architectures. 2-Dimensional materials, such as transition metal dichalcogenides (TMDs), may serve as a materials platform to improve HTLs without excess parasitic absorption and carrier generation outside of the PbS CQD absorbing layer due to their extreme thinness. Additionally, many of the reported values for mobilities in these layers used in both simulation and experiments are derived from either the SCLC method or field effect transistor measurements. These values represent lateral/in-plane carrier mobilities, whereas transport typically occurs in the vertical direction in solar cells. A more extensive understanding of potential transport anisotropy in PbS CQD films and related materials used as HTLs could serve to align simulated and experimental device performance.

(2) Surface and interface chemistry. Another important challenge in improving PbS CQD photovoltaics is the introduction of electronic and optical losses at interfaces between the solar cell layers. To realize large-area PbS CQD devices, new interface engineering methods must be compatible with scalable fabrication processes and ambient temperatures. Much research has shown that altering surface ligands can improve electronic performance in films, with mixed-halide passivation as a successful example of this strategy. In the context of tandem solar cells, the ratios of exposed surface areas of different crystal planes on different sized PbS CQDs (1 eV for tandem NIR cells) are different than in single junction 1.3 eV quantum dot solar cells. Therefore, these devices could require different precursor ratios to passivate the films and improve charge transport. An open area of exploration is specific ligand exchanges or the introduction of self-assembled monolayers at the interfaces between, *e.g.*, the PbS CQD photovoltaic film and the charge transport layers and contacts. While perovskite monolayer passivation has shown the biggest improvements in efficiency, the formamidinium iodide precursor is significantly more expensive than lead halide salts. An economic analysis of the scaling of solar cells based on these materials should be performed. Other benefits of interface engineering may include improvement in long-term stability and reduced air and water sensitivity, necessary for the widespread deployment of these devices under real operating conditions. As is standard practice in the field, most literature uses AM1.5G illumination testing conditions, but real operating conditions fluctuate significantly and impact the amount of power these devices can output over the course of a day. It is imperative that PCE information under outdoor testing gets collected at a variety of operating conditions, as different illumination and temperature conditions can significantly impact film properties such as carrier mobilities, diffusion lengths, and photo-passivated trap state densities.

(3) Scaling fabrication. While solutions of PbS CQDs have reached sufficient synthetic quality at scale for commercialization, fabrication methods for full solar cells that maintain lab-scale efficiency have not yet been demonstrated. Traditional processes from the printing industry such as blade-coating or roll-to-roll printing are viable options; however, producing consistently high-quality electronic films from such processes remains a challenge. Passivation chemistries that can be achieved at near ambient temperature and pressure conditions that are compatible with these techniques are crucial, as mentioned above. Borrowing the already scaled manufacturing practices used for quantum dot televisions could provide a pathway to large volume synthesis of quantum dots and fabrication of electronics with commercially viable performance for building-integrated photovoltaics and other applications.

(4) Recycling and circularity. In recent years, the idea of circular economies and ensuring that the total lifecycle of products includes recycling or upcycling back into working devices at the end of their initial lifetimes has gained much attention in the larger photovoltaics community.[136,137] A techno-economic analysis and understanding of ways to reclaim materials from colloidal quantum dot solar cells would be of great interest, as the techniques in the growing field of silicon solar cell recycling would not be directly compatible with colloidal material devices. Incineration as an alternative to recycling is not an option for lead-containing devices. Possible reprocessing options include chemical stripping of various layers and subsequent electrolysis of the lead and zinc back

into elemental form. In addition to recycling, an open area of research interest is PbS CQD solar cell degradation mechanisms and compounds during operation for environmental or health-related remediation.

(5) Alternative non-toxic-material quantum dots. PbS is considered a 'probable carcinogen' in bulk form, but in quantum dot form, PbS–MPA has been found to have a link to carcinogenic activity in human cells.[138] There have been recent reports of using Ag-based quantum dots such as $Ag_2S$[139] and more recently AgBiS[140,141] for NIR absorption in solar cells. These materials offer a potentially non-toxic alternative to the lead-based quantum dots discussed in this article, and have reached above 9% power conversion efficiency in devices. For these devices to reach efficiencies as high as those achieved with PbS quantum dots, similar strategies for passivation and charge transport engineering need to be explored.

We have discussed various strategies that highlight the modularity of PbS CQD photovoltaics and their tailorable properties as NIR absorbers, a difficult spectral regime of high interest for photovoltaic and energy systems. From custom optical properties of both CQD films and devices, and with the rapid development of nanoparticle synthetic, fabrication, and characterization methods, the mechanisms for performance losses – and solutions to mitigate them – can be explored and developed with a renewed focus, ultimately leading to the development of scalable PV systems for new applications to broaden the reach of solar energy.

## Author contributions

Conceptualization: Sreyas Chintapalli, Lulin Li, Susanna Thon; data curation: Sreyas Chintapalli and Lulin Li; formal analysis: Sreyas Chintapalli; funding acquisition: Susanna Thon; investigation: Sreyas Chintapalli and Lulin Li; methodology: Sreyas Chintapalli and Lulin Li; project administration: Susanna Thon; resources: Susanna Thon; software: Sreyas Chintapalli; supervision: Susanna Thon; validation: Sreyas Chintapalli and Lulin Li; visualization: Sreyas Chintapalli; writing – original draft: Sreyas Chintapalli, Lulin Li, Susanna Thon; writing – review & editing: Sreyas Chintapalli and Susanna Thon.

## Conflicts of interest

There are no conflicts to declare.

## Data availability

No primary research results, software or code have been included and no new data were generated or analysed as part of this review.

## Acknowledgements

This work was supported by the National Science Foundation (DMR-1807342, ECCS-1846239, DGE-2346004), the U.S. Department of Defense (W911NF2120213) and the Ralph O'Connor Sustainable Energy Institute at Johns Hopkins University.

## References

1 E. A. Wrigley, *Philos. Trans. R. Soc., A*, 2013, **371**, 20110568.
2 D. Welsby, J. Price, S. Pye and P. Ekins, *Nature*, 2021, **597**, 230–234.
3 R. Wolniak and B. Skotnicka-Zasadzień, *Energies*, 2022, **15**, 662.
4 W. Palosz, S. Trivedi, E. DeCuir, P. S. Wijewarnasuriya, S. M. Thon, Y. Cheng, C. Lu and J. L. Jensen, *Part. Part. Syst. Charact.*, 2021, **38**, 2000285.
5 M. Perez and R. Perez, *Sol. Energy Adv.*, 2022, **2**, 100014.
6 S. P. Bremner, M. Y. Levy and C. B. Honsberg, *Prog. Photovoltaics Res. Appl.*, 2008, **16**, 225–233.
7 T. Mambrini, A. M. Dubois, C. Longeaud, J. Badosa, M. Haeffelin, L. Prieur and V. Radivoniuk, *EPJ Photovoltaics*, 2015, **6**, 60701.
8 W. Shockley and H. J. Queisser, *J. Appl. Phys.*, 1961, **32**, 510–519.
9 Y. Xu, T. Gong and J. N. Munday, *Sci. Rep.*, 2015, **5**, 13536.
10 J. N. Munday, *J. Appl. Phys.*, 2012, **112**, 064501.
11 B. Ehrler, E. Alarcón-Lladó, S. W. Tabernig, T. Veeken, E. C. Garnett and A. Polman, *ACS Energy Lett.*, 2020, **5**, 3029–3033.
12 P. Würfel and U. Würfel, *Physics of solar cells: from basic principles to advanced concepts*, Wiley-VCH, Weinheim, 2nd edn, 2009.
13 F. Wang, J. Wang and X. Liu, *Angew. Chem., Int. Ed.*, 2010, **49**, 7456–7460.
14 L. C. Hirst and N. J. Ekins-Daukes, *Prog. Photovoltaics Res. Appl.*, 2011, **19**, 286–293.
15 H. Lian, Z. Hou, M. Shang, D. Geng, Y. Zhang and J. Lin, *Energy*, 2013, **57**, 270–283.
16 O. Andersson and M. Kemerink, *Sol. RRL*, 2020, **4**, 2000400.
17 N. Sawala, K. Koparkar, N. Bajaj and S. Omanwar, *Optik*, 2016, **127**, 4375–4378.
18 A. Husain, G. Kumar and M. Nazim, *Advances in Electronic Materials for Clean Energy Conversion and Storage Applications*, Elsevier, 2023, pp. 265–280.
19 X. Wang, G. I. Koleilat, J. Tang, H. Liu, I. J. Kramer, R. Debnath, L. Brzozowski, D. A. R. Barkhouse, L. Levina, S. Hoogland and E. H. Sargent, *Nat. Photonics*, 2011, **5**, 480–484.
20 H. Wang, T. Kubo, J. Nakazaki and H. Segawa, *ACS Energy Lett.*, 2017, **2**, 2110–2117.
21 X. Jiang, M. Sun, Z. Chen, J. Jing and C. Feng, *Corros. Sci.*, 2020, **176**, 108901.
22 N. S. Beattie, P. See, G. Zoppi, P. M. Ushasree, M. Duchamp, I. Farrer, D. A. Ritchie and S. Tomic, *ACS Photonics*, 2017, **4**, 2745–2750.
23 A. Martí, N. López, E. Antolín, E. Cánovas, C. Stanley, C. Farmer, L. Cuadra and A. Luque, *Thin Solid Films*, 2006, **511–512**, 638–644.
24 J. Li, S. Zhang, H. Luo, Z. Mu, Z. Li, Q. Du, J. Feng and F. Wu, *Opt. Mater.*, 2018, **85**, 523–530.
25 D. Fang, X. Zhang, C. Zhao, X. Liu, X. Shu and J. Wang, *Opt. Mater.*, 2019, **88**, 80–90.
26 L. C. Hirst, H. Fujii, Y. Wang, M. Sugiyama and N. J. Ekins-Daukes, *IEEE J. Photovolt.*, 2014, **4**, 244–252.
27 Z.-C. Su, C.-H. Chang, J.-C. Jhou, H.-T. Lin and C.-F. Lin, *Sci. Rep.*, 2023, **13**, 5388.
28 K. K. Paul, J.-H. Kim and Y. H. Lee, *Nat. Rev. Phys.*, 2021, **3**, 178–192.
29 N. J. L. K. Davis, M. L. Böhm, M. Tabachnyk, F. Wisnivesky-Rocca-Rivarola, T. C. Jellicoe, C. Ducati, B. Ehrler and N. C. Greenham, *Nat. Commun.*, 2015, **6**, 8259.
30 X. Jiang, R. D. Schaller, S. B. Lee, J. M. Pietryga, V. I. Klimov and A. A. Zakhidov, *J. Mater. Res.*, 2007, **22**, 2204–2210.
31 F. W. Wise, *Acc. Chem. Res.*, 2000, **33**, 773–780.
32 M. Thambidurai, N. Muthukumarasamy, S. Agilan, N. Murugan, S. Vasantha, R. Balasundaraprabhu and T. S. Senthil, *J. Mater. Sci.*, 2010, **45**, 3254–3258.
33 M. S. Zaini, J. Ying Chyi Liew, S. A. Alang Ahmad, A. R. Mohmad and M. A. Kamarudin, *Appl. Sci.*, 2020, **10**, 6282.
34 T. Takagahara and K. Takeda, *Phys. Rev. B:Condens. Matter Mater. Phys.*, 1992, **46**, 15578–15581.

 

35 P. Harrison and A. Valavanis, *Quantum wells, wires and dots: theoretical and computational physics of semiconductor nanostructures*, Wiley, Chichester, West Sussex, United Kingdom; Hoboken, NJ, USA, 4th edn, 2016.
36 E. H. Sargent, *Adv. Mater.*, 2005, **17**, 515–522.
37 K. S. Jeong, J. Tang, H. Liu, J. Kim, A. W. Schaefer, K. Kemp, L. Levina, X. Wang, S. Hoogland, R. Debnath, L. Brzozowski, E. H. Sargent and J. B. Asbury, *ACS Nano*, 2012, **6**, 89–99.
38 J. Ramade, J. Qu, A. Chu, C. Gréboval, C. Livache, N. Goubet, B. Martinez, G. Vincent and E. Lhuillier, *ACS Photonics*, 2020, **7**, 272–278.
39 *Efficient Infrared Electroluminescent Devices Using Solution-Processed Colloidal Quantum Dots – Konstantatos – 2005 – Advanced Functional Materials – Wiley Online Library*, DOI: 10.1002/adfm.200500379.
40 R. A. Oliver, G. A. D. Briggs, M. J. Kappers, C. J. Humphreys, S. Yasin, J. H. Rice, J. D. Smith and R. A. Taylor, *Appl. Phys. Lett.*, 2003, **83**, 755–757.
41 H. Lipsanen, M. Sopanen and J. Ahopelto, *Phys. Rev. B:Condens. Matter Mater. Phys.*, 1995, **51**, 13868–13871.
42 K. I. Hunter, J. T. Held, K. A. Mkhoyan and U. R. Kortshagen, *ACS Appl. Mater. Interfaces*, 2017, **9**, 8263–8270.
43 Y. Wei, H. Yu, H. Li, H. Ming, K. Pan, H. Huang, Y. Liu and Z. Kang, *Mater. Res. Bull.*, 2013, **48**, 4072–4077.
44 N. Sukharevska, D. Bederak, V. M. Goossens, J. Momand, H. Duim, D. N. Dirin, M. V. Kovalenko, B. J. Kooi and M. A. Loi, *ACS Appl. Mater. Interfaces*, 2021, **13**, 5195–5207.
45 S. Zhou, Z. Liu, Y. Wang, K. Lu, F. Yang, M. Gu, Y. Xu, S. Chen, X. Ling, Y. Zhang, F. Li, J. Yuan and W. Ma, *J. Mater. Chem. C*, 2019, **7**, 1575–1583.
46 H. Wang, W. Yao, Q. Tian, M. Li, B. Tian, L. Liu, Z. Wu and W. Wu, *Adv. Mater. Technol.*, 2018, **3**, 1800150.
47 S. Ali, J. Bae, C. H. Lee, K. H. Choi and Y. H. Doh, *Org. Electron.*, 2015, **25**, 225–231.
48 N. Sukharevska, D. Bederak, V. M. Goossens, J. Momand, H. Duim, D. N. Dirin, M. V. Kovalenko, B. J. Kooi and M. A. Loi, *ACS Appl. Mater. Interfaces*, 2021, **13**, 5195–5207.
49 J. Z. Fan, M. Vafaie, K. Bertens, M. Sytnyk, J. M. Pina, L. K. Sagar, O. Ouellette, A. H. Proppe, A. S. Rasouli, Y. Gao, S.-W. Baek, B. Chen, F. Laquai, S. Hoogland, F. P. G. D. Arquer, W. Heiss and E. H. Sargent, *Nano Lett.*, 2020, **20**, 5284–5291.
50 H. Yu, J. Zhang, T. Long, M. Xu, H. Feng, L. Zhang, S. Liu and W. Xie, *J. Phys. Chem. Lett.*, 2020, **11**, 9019–9025.
51 L. Li, B. Qiu, C. Lu, L. Shimabukuro, Y. Lin and S. M. Thon, 2019 IEEE 46th Photovoltaic Specialists Conference (PVSC), 2019, pp. 0015–0018.
52 I. J. Kramer, J. C. Minor, G. Moreno-Bautista, L. Rollny, P. Kanjanaboos, D. Kopilovic, S. M. Thon, G. H. Carey, K. W. Chou, D. Zhitomirsky, A. Amassian and E. H. Sargent, *Adv. Mater.*, 2015, **27**, 116–121.
53 J. Yuan, C. Bi, S. Wang, R. Guo, T. Shen, L. Zhang and J. Tian, *Adv. Funct. Mater.*, 2019, **29**, 1906615.
54 V. Khoshdel, M. Joodaki and M. Shokooh-Saremi, *Opt. Commun.*, 2019, **433**, 275–282.
55 S. Moon, K. Kim, Y. Kim, J. Heo and J. Lee, *Sci. Rep.*, 2016, **6**, 30107.
56 X. Zhang, V. A. Öberg, J. Du, J. Liu and E. M. J. Johansson, *Energy Environ. Sci.*, 2018, **11**, 354–364.
57 J. Kim, G. Kim, H. Back, J. Kong, I.-W. Hwang, T. K. Kim, S. Kwon, J.-H. Lee, J. Lee, K. Yu, C.-L. Lee, H. Kang and K. Lee, *Adv. Mater.*, 2016, **28**, 3159–3165.
58 J. M. Luther, J. Gao, M. T. Lloyd, O. E. Semonin, M. C. Beard and A. J. Nozik, *Adv. Mater.*, 2010, **22**, 3704–3707.
59 C.-H. M. Chuang, P. R. Brown, V. Bulovic and M. G. Bawendi, *Nat. Mater.*, 2014, **13**, 796–801.
60 X. Lan, O. Voznyy, A. Kiani, F. P. García De Arquer, A. S. Abbas, G. Kim, M. Liu, Z. Yang, G. Walters, J. Xu, M. Yuan, Z. Ning, F. Fan, P. Kanjanaboos, I. Kramer, D. Zhitomirsky, P. Lee, A. Perelgut, S. Hoogland and E. H. Sargent, *Adv. Mater.*, 2016, **28**, 299–304.
61 J. Z. Fan, N. T. Andersen, M. Biondi, P. Todorović, B. Sun, O. Ouellette, J. Abed, L. K. Sagar, M. Choi, S. Hoogland, F. P. G. De Arquer and E. H. Sargent, *Adv. Mater.*, 2019, **31**, 1904304.
62 C. Ding, D. Wang, D. Liu, H. Li, Y. Li, S. Hayase, T. Sogabe, T. Masuda, Y. Zhou, Y. Yao, Z. Zou, R. Wang and Q. Shen, *Adv. Energy Mater.*, 2022, **12**, 2201676.
63 T. Huang, C. Wu, J. Yang, P. Hu, L. Qian, T. Sun and C. Xiang, *ACS Appl. Mater. Interfaces*, 2024, **16**, 915–923.
64 B. Sun, A. Johnston, C. Xu, M. Wei, Z. Huang, Z. Jiang, H. Zhou, Y. Gao, Y. Dong, O. Ouellette, X. Zheng, J. Liu, M.-J. Choi, Y. Gao, S.-W. Baek, F. Laquai, O. M. Bakr, D. Ban, O. Voznyy, F. P. García De Arquer and E. H. Sargent, *Joule*, 2020, **4**, 1542–1556.
65 X. Meng, Y. Chen, F. Yang, J. Zhang, G. Shi, Y. Zhang, H. Tang, W. Chen, Y. Liu, L. Yuan, S. Li, K. Wang, Q. Chen, Z. Liu and W. Ma, *Nano Res.*, 2022, **15**, 6121–6127.
66 R. Dantas Campos, S. Singh, H. Heffner, M. Löffler, F. Paulus and Y. Vaynzof, *J. Mater. Chem. A*, 2024, **12**, 32689–32696.
67 G. Shi, X. Ding, Z. Liu, Y. Liu, Y. Chen, C. Liu, Z. Ni, H. Wang, K. Ito, K. Igarashi, K. Feng, K. Zhang, L. Lüer, W. Chen, X. Lyu, B. Song, X. Sun, L. Yuan, D. Liu, Y. Li, K. Lu, W. Deng, Y. Li, P. Müller-Buschbaum, T. Li, J. Zhong, S. Uchida, T. Kubo, N. Li, J. M. Luther, H. Segawa, Q. Shen, C. J. Brabec and W. Ma, *Nat. Energy*, 2025, **10**, 592–604.
68 H. Aqoma, S.-H. Lee, I. F. Imran, J.-H. Hwang, S.-H. Lee and S.-Y. Jang, *Nat. Energy*, 2024, **9**, 324–332.
69 A. H. Ip, S. M. Thon, S. Hoogland, O. Voznyy, D. Zhitomirsky, R. Debnath, L. Levina, L. R. Rollny, G. H. Carey, A. Fischer, K. W. Kemp, I. J. Kramer, Z. Ning, A. J. Labelle, K. W. Chou, A. Amassian and E. H. Sargent, *Nat. Nanotechnol.*, 2012, **7**, 577–582.
70 X. Lan, O. Voznyy, F. P. García De Arquer, M. Liu, J. Xu, A. H. Proppe, G. Walters, F. Fan, H. Tan, M. Liu, Z. Yang, S. Hoogland and E. H. Sargent, *Nano Lett.*, 2016, **16**, 4630–4634.
71 J. Xu, O. Voznyy, M. Liu, A. R. Kirmani, G. Walters, R. Munir, M. Abdelsamie, A. H. Proppe, A. Sarkar, F. P. García De Arquer, M. Wei, B. Sun, M. Liu, O. Ouellette, R. Quintero-Bermudez, J. Li, J. Fan, L. Quan, P. Todorovic, H. Tan, S. Hoogland, S. O. Kelley, M. Stefik, A. Amassian and E. H. Sargent, *Nat. Nanotechnol.*, 2018, **13**, 456–462.
72 Y. Liu, H. Wu, G. Shi, Y. Li, Y. Gao, S. Fang, H. Tang, W. Chen, T. Ma, I. Khan, K. Wang, C. Wang, X. Li, Q. Shen, Z. Liu and W. Ma, *Adv. Mater.*, 2023, **35**, 2207293.
73 C. Kim, I. Kozakci, S. Y. Lee, B. Kim, J. Kim, J. Lee, B. S. Ma, E. S. Oh, T. Kim and J. Lee, *Small*, 2023, **19**, 2302195.
74 J. Li, X. Zhang, Z. Liu, H. Wu, A. Wang, Z. Luo, J. Wang, W. Dong, C. Wang, S. Wen, Q. Dong, W. W. Yu and W. Zheng, *Small*, 2024, **20**, 2311461.
75 L. Zhang, Y. Chen, S. Cao, D. Yuan, X. Tang, D. Wang, Y. Gao, J. Zhang, Y. Zhao, X. Yang, Z. Lu, Q. Fan and B. Sun, *Adv. Sci.*, 2024, **11**, 2402756.
76 X. Wen, C. Gao, X. Ding, G. Shi, X. Yuan, B. Li, L. Yuan, J. Guo, C. Duan, Q. Shen, W. Ma and Z. Liu, *Adv. Mater.*, 2025, 2500562.
77 *CRC Handbook of Chemistry and Physics*, ed. W. M. Haynes, CRC Press, Boca Raton, 97th edn, 2016.
78 S. Chan, M. Liu, K. Latham, M. Haruta, H. Kurata, T. Teranishi and Y. Tachibana, *J. Mater. Chem. C*, 2017, **5**, 2182–2187.
79 C. R. Kagan, E. Lifshitz, E. H. Sargent and D. V. Talapin, *Science*, 2016, **353**, aac5523.
80 I. Moreels, K. Lambert, D. Smeets, D. De Muynck, T. Nollet, J. C. Martins, F. Vanhaecke, A. Vantomme, C. Delerue, G. Allan and Z. Hens, *ACS Nano*, 2009, **3**, 3023–3030.
81 L. Brus, *J. Phys. Chem.*, 1986, **90**, 2555–2560.
82 L. Cademartiri, E. Montanari, G. Calestani, A. Migliori, A. Guagliardi and G. A. Ozin, *J. Am. Chem. Soc.*, 2006, **128**, 10337–10346.
83 N. Borrelli and D. Smith, *J. Non-Cryst. Solids*, 1994, **180**, 25–31.
84 R. S. Kane, R. E. Cohen and R. Silbey, *J. Phys. Chem.*, 1996, **100**, 7928–7932.
85 M. Hines and G. Scholes, *Adv. Mater.*, 2003, **15**, 1844–1849.
86 B. Hou, Y. Cho, B. S. Kim, J. Hong, J. B. Park, S. J. Ahn, J. I. Sohn, S. Cha and J. M. Kim, *ACS Energy Lett.*, 2016, **1**, 834–839.
87 A. R. Kirmani, *MRS Bull.*, 2019, **44**, 524–525.
88 S. G. Kwon, Y. Piao, J. Park, S. Angappane, Y. Jo, N.-M. Hwang, J.-G. Park and T. Hyeon, *J. Am. Chem. Soc.*, 2007, **129**, 12571–12584.
89 J. Zhang, R. W. Crisp, J. Gao, D. M. Kroupa, M. C. Beard and J. M. Luther, *J. Phys. Chem. Lett.*, 2015, **6**, 1830–1833.
90 Y. Wang, Z. Liu, N. Huo, F. Li, M. Gu, X. Ling, Y. Zhang, K. Lu, L. Han, H. Fang, A. G. Shulga, Y. Xue, S. Zhou, F. Yang, X. Tang, J. Zheng, M. Antonietta Loi, G. Konstantatos and W. Ma, *Nat. Commun.*, 2019, **10**, 5136.
91 X. Ding, X. Wen, Y. Kawata, Y. Liu, G. Shi, R. B. Ghazi, X. Sun, Y. Zhu, H. Wu, H. Gao, Q. Shen, Z. Liu and W. Ma, *Nanoscale*, 2024, **16**, 5115–5122.

92 A. Paliwal, S. V. Singh, A. Sharma, A. Sugathan, S.-W. Liu, S. Biring and B. N. Pal, *ACS Appl. Nano Mater.*, 2018, **1**, 6063–6072.
93 Y. Choi, N. Thongsai, A. Chae, S. Jo, E. B. Kang, P. Paoprasert, S. Park and I. In, *J. Ind. Eng. Chem.*, 2016, **47**, 329–335.
94 D. Vanmaekelbergh and P. Liljeroth, *Chem. Soc. Rev.*, 2005, **34**, 299.
95 I. Moreels, B. Fritzinger, J. C. Martins and Z. Hens, *J. Am. Chem. Soc.*, 2008, **130**, 15081–15086.
96 M. Liu, O. Voznyy, R. Sabatini, F. P. García De Arquer, R. Munir, A. H. Balawi, X. Lan, F. Fan, G. Walters, A. R. Kirmani, S. Hoogland, F. Laquai, A. Amassian and E. H. Sargent, *Nat. Mater.*, 2017, **16**, 258–263.
97 Z. Ning, H. Dong, Q. Zhang, O. Voznyy and E. H. Sargent, *ACS Nano*, 2014, **8**, 10321–10327.
98 D. Jia, J. Chen, S. Zheng, D. Phuyal, M. Yu, L. Tian, J. Liu, O. Karis, H. Rensmo, E. M. J. Johansson and X. Zhang, *Adv. Energy Mater.*, 2019, **9**, 1902809.
99 National Renewable Energy Laboratory (NREL), *Best research-cell efficiency chart*, 2024, **https://www.nrel.gov/pv/cell-efficiency.html**.
100 H. Aqoma, S.-H. Lee, I. F. Imran, J.-H. Hwang, S.-H. Lee and S.-Y. Jang, *Nat. Energy*, 2024, **9**, 324–332.
101 A. Chiu, E. Rong, C. Bambini, Y. Lin, C. Lu and S. M. Thon, *ACS Energy Lett.*, 2020, **5**, 2897–2904.
102 A. Chiu, C. Lu, D. E. Kachman, E. Rong, S. M. Chintapalli, Y. Lin, D. Khurgin and S. M. Thon, *Nanoscale*, 2024, **16**, 8273–8285.
103 V. M. Le Corre, E. A. Duijnstee, O. El Tambouli, J. M. Ball, H. J. Snaith, J. Lim and L. J. A. Koster, *ACS Energy Lett.*, 2021, **6**, 1087–1094.
104 L. Hu, Q. Lei, X. Guan, R. Patterson, J. Yuan, C. Lin, J. Kim, X. Geng, A. Younis, X. Wu, X. Liu, T. Wan, D. Chu, T. Wu and S. Huang, *Adv. Sci.*, 2021, **8**, 2003138.
105 Y. Lin, T. Gao, X. Pan, M. Kamenetska and S. M. Thon, *Adv. Mater.*, 2020, **32**, 1906602.
106 M. Saliba, K. W. Tan, H. Sai, D. T. Moore, T. Scott, W. Zhang, L. A. Estroff, U. Wiesner and H. J. Snaith, *J. Phys. Chem. C*, 2014, **118**, 17171–17177.
107 C. G. Shuttle, B. O'Regan, A. M. Ballantyne, J. Nelson, D. D. C. Bradley, J. De Mello and J. R. Durrant, *Appl. Phys. Lett.*, 2008, **92**, 093311.
108 H. J. Lee, A. B. Hofelmann, Y. Lin and S. M. Thon, 2022 IEEE 49th Photovoltaics Specialists Conference (PVSC), Philadelphia, PA, USA, 2022, pp. 0862–0866.
109 H. J. Lee, A. Chiu, Y. Lin, S. Chintapalli, S. Kamal, E. Ji and S. M. Thon, *Adv. Intell. Syst.*, 2024, 2400310.
110 A. G. Hestnes, *Sol. Energy*, 1999, **67**, 181–187.
111 A. Henemann, *Renewable Energy Focus*, 2008, **9**, 14–19.
112 E. S. Arinze, B. Qiu, N. Palmquist, Y. Cheng, Y. Lin, G. Nyirjesy, G. Qian and S. M. Thon, *Opt. Express*, 2017, **25**, A101.
113 B. Qiu, E. S. Arinze, N. Palmquist, Y. Cheng, Y. Lin, G. Nyirjesy, G. Qian and S. M. Thon, Conference on Lasers and Electro-Optics, San Jose, California, 2017, p. SM4K.5.
114 A. Røyset, T. Kolås and B. P. Jelle, *Energy Build.*, 2020, **208**, 109623.
115 B. Li, B. Hou and G. A. J. Amaratunga, *InfoMat*, 2021, **3**, 445–459.
116 B. Qiu, Y. Lin, E. S. Arinze, A. Chiu, L. Li and S. M. Thon, *Opt. Express*, 2018, **26**, 26933.
117 A. Chiu, B. Qiu, Y. Lin, E. S. Arinze, L. Li and S. M. Thon, 2019 IEEE 46th Photovoltaic Specialists Conference (PVSC), Chicago, IL, USA, 2019, pp. 0004–0007.
118 Y. Kim, K. Bicanic, H. Tan, O. Ouellette, B. R. Sutherland, F. P. García De Arquer, J. W. Jo, M. Liu, B. Sun, M. Liu, S. Hoogland and E. H. Sargent, *Nano Lett.*, 2017, **17**, 2349–2353.
119 S. M. Chintapalli, T. Gao, A. Chiu, Y. Lin and S. M. Thon, *OSA Advanced Photonics Congress 2021*, Washington, DC, 2021, p. PvM2B.4.
120 Z. Liu, D. Zhu, L. Raju and W. Cai, *Adv. Sci.*, 2021, **8**, 2002923.
121 S. Chintapalli, T. Gao, L. Singh, S. Kamal, A. Chiu, Y. Zhang and S. M. Thon, 2023 IEEE 50th Photovoltaic Specialists Conference (PVSC), San Juan, PR, USA, 2023, pp. 1–3.
122 A. D. Vos, *J. Phys. D: Appl. Phys.*, 1980, **13**, 839–846.
123 B. Sun, A. T. Findikoglu, M. Sykora, D. J. Werder and V. I. Klimov, *Nano Lett.*, 2009, **9**, 1235–1241.
124 D. Wang, H. Yang, J. Duan, W. Liu and H. Wu, *IEEE Trans. Electron Devices*, 2023, 1–6.
125 M. Raissi, Y. Pellegrin, S. Jobic, M. Boujtita and F. Odobel, *Sci. Rep.*, 2016, **6**, 24908.
126 Y. Zhang, M. Gu, N. Li, Y. Xu, X. Ling, Y. Wang, S. Zhou, F. Li, F. Yang, K. Ji, J. Yuan and W. Ma, *J. Mater. Chem. A*, 2018, **6**, 24693–24701.
127 M. M. Tavakoli, H. T. Dastjerdi, P. Yadav, D. Prochowicz, H. Si and R. Tavakoli, *Adv. Funct. Mater.*, 2021, **31**, 2010623.
128 A. Andruszkiewicz, X. Zhang, M. B. Johansson, L. Yuan and E. M. J. Johansson, *Nanoscale*, 2021, **13**, 6234–6240.
129 A. Manekkathodi, B. Chen, J. Kim, S.-W. Baek, B. Scheffel, Y. Hou, O. Ouellette, M. I. Saidaminov, O. Voznyy, V. E. Madhavan, A. Belaidi, S. Ashhab and E. Sargent, *J. Mater. Chem. A*, 2019, **7**, 26020–26028.
130 M. J. Speirs, B. G. H. M. Groeneveld, L. Protesescu, C. Piliego, M. V. Kovalenko and M. A. Loi, *Phys. Chem. Chem. Phys.*, 2014, **16**, 7672–7676.
131 T. Kim, Y. Gao, H. Hu, B. Yan, Z. Ning, L. K. Jagadamma, K. Zhao, A. R. Kirmani, J. Eid, M. M. Adachi, E. H. Sargent, P. M. Beaujuge and A. Amassian, *Nano Energy*, 2015, **17**, 196–205.
132 G. Shi, Y. Wang, Z. Liu, L. Han, J. Liu, Y. Wang, K. Lu, S. Chen, X. Ling, Y. Li, S. Cheng and W. Ma, *Adv. Energy Mater.*, 2017, **7**, 1602667.
133 Y. Gao, J. Zheng, W. Chen, L. Yuan, Z. L. Teh, J. Yang, X. Cui, G. Conibeer, R. Patterson and S. Huang, *J. Phys. Chem. Lett.*, 2019, **10**, 5729–5734.
134 Y.-L. Li, P.-N. Yeh, S. Sharma and S.-A. Chen, *J. Mater. Chem. A*, 2017, **5**, 21528–21535.
135 L. Li, B. Qiu, Y. Lin, L. Shimabukuro, A. Ozbolt, K. K. Yao, S. Farias, S. Rosenthal and S. M. Thon, 2023 IEEE 50th Photovoltaic Specialists Conference (PVSC), San Juan, PR, USA, 2023, pp. 1–3.
136 K. M. Kennedy, S. M. Chintapalli, B. Phelps, S. Vo, S. Smith, S. Thon and N. Hultman, *A circular economy approach to solar photovoltaics in maryland*, Center for global sustainability, university of maryland & ralph o'connor sustainable energy institute, johns hopkins university report, 2024.
137 R. G. Charles, A. Doolin, R. García-Rodríguez, K. V. Villalobos and M. L. Davies, *Energy Environ. Sci.*, 2023, **16**, 3711–3733.
138 E. Kim, J.-H. Kim, H.-R. Kim, B.-R. Lee, E.-S. Choi and S.-I. In, *Int. J. Nanomed.*, 2015, 5513.
139 J. Xue, J. Liu, S. Mao, Y. Wang, W. Shen, W. Wang, L. Huang, H. Li and J. Tang, *Mater. Res. Bull.*, 2018, **106**, 113–123.
140 C. Kim, I. Kozakci, J. Kim, S. Y. Lee and J. Lee, *Adv. Energy Mater.*, 2022, **12**, 2200262.
141 F. A. N. Mawaddah and S. Z. Bisri, *Nanomaterials*, 2024, **14**, 1328.

 